SCIENTIFIC REP♦RTS

OPEN

Structure, Intrinsic properties and Vibrational Spectra of Pr(Mg$_{1/2}$Sn$_{1/2}$)O$_3$ Ceramic Crystal

Hengyang Qiao[1], Haiqing Sun[1], Jianzhu Li[1], Huiling Chen[1], Chao Xing[1], Jun Yang[1], Helei Dong[2], Jing Wang[1], Xunqian Yin[1], Ze-Ming Qi[3] & Feng Shi[1,4]

Pr(Mg$_{1/2}$Sn$_{1/2}$)O$_3$ (PMS) ceramic was prepared through a conventional solid-state reaction method. Crystal structure was investigated through X-ray diffraction (XRD), which certificates that the main phase is PMS with monoclinic *P2$_1$/n1* symmetry. Lattice vibrational modes were obtained through Raman scattering spectroscopy and Fourier transform far-infrared reflection spectroscopy. The Raman spectrum active modes were assigned and illustrated, respectively, and then fitted with Lorentzian function. The four modes within the range of 110–200 cm^{-1} are derived from the F_{2g} vibrations (A-site cations), and the other three modes (300–430 cm^{-1}) are derived from the F_{2g} vibrations (B-site cations). The mode with highest frequency above 650 cm^{-1} is attributed to A_{1g}-like mode that corresponds to the symmetric breathing of oxygen octahedral. The far-infrared spectrum with seven infrared active modes was fitted using four-parameter semi-quantum models to calculate intrinsic properties (permittivity and loss). $F_{2u}^{(2)}$ yielded the greatest contribution to dielectric constant and loss, which is mainly performed as the inverted translational vibration of Pr-MgO$_6$ octahedron.

In recent years, the mobile communication develops to high reliability with small size, then higher requirements are put forward for microwave dielectric ceramics (MWDCs). Thanks to the suitable permittivities (ε), high-quality factors (Q), and near-zero temperature coefficient of resonant frequency (τ_f), $A(B'_{1/2}B''_{1/2})O_3$-type MWDCs are widely applied in resonators and filters. Rare-earth based MWDCs with double perovskites structure have been considered as potential candidate to substitute expensive complex perovskite MWDCs like Ba(Mg$_{1/3}$Ta$_{2/3}$)O$_3$, which have been applied in commerce. Among these materials, Pr(Mg$_{1/2}$Sn$_{1/2}$)O$_3$ (PMS) ceramics is promising with excellent properties in high frequency band of microwave frequency region.

Recently, more and more rare-earth based MWDCs, such as La(Mg$_{1/2}$Ti$_{1/2}$)O$_3$, La(Zn$_{1/2}$Ti$_{1/2}$)O$_3$ and La(Mg$_{1/2}$Sn$_{1/2}$)O$_3$ had been widely studied[1–4]. The research of these ceramic materials mainly focuses on the basic structures[5,6], lower the sintering temperatures[7,8] and add additives to improve dielectric properties[9]. For example, crystal structures, dielectric properties and vibrational spectra of La(Mg$_{1/2}$Sn$_{1/2}$)O$_3$ and La(Mg$_{1/2}$Ti$_{1/2}$)O$_3$ ceramics were studied by Babu *et al.*[10,11], which confirmed that these ceramics are the B-site ordered monoclinic crystal with space group *P2$_1$/n1*. Subsequently, Chen *et al.* studied La(Mg$_{1/2}$Sn$_{1/2}$)O$_3$ and Nd(Mg$_{1/2}$Sn$_{1/2}$)O$_3$ ceramic doped with a variety of materials such as ZnO-B$_2$O$_3$-SiO$_2$[1], B$_2$O$_3$[12,13], Yb$_2$O[14], ZnO[15], and V$_2$O$_5$[16].

There are many researches on praseodymium based materials, for example, to study the GMR properties of praseodymium based perovskites Pr$_{0.7}$(Sr, Ca)$_{0.3}$Mn$_{1−x}$Al$_x$O$_3$ and Pr$_{0.5}$Sr$_{0.5}$Mn$_{1−x}$Al$_x$O$_3$[17], to study the catalytic properties of Pr$_{0.4}$Ba$_{0.4}$Ce$_{0.2}$SrNiO$_4$[18], and to study the relationship between thermal expansion and oxygen ion transport of A$_{1−a}$A$_a$'BO$_3$ perovskite-type oxides[19].

However, there is no research on praseodymium based perovskites MWDCs up to date, for example, Pr(Mg$_{1/2}$Sn$_{1/2}$)O$_3$ (PMS). Especially, applying both Raman scattering spectroscopy and Fourier transform far-infrared reflection spectroscopy together to investigate the vibrator parameters and the intrinsic properties of PMS is still unknown.

[1]School of Material Science & Engineering, Shandong University of Science and Technology, Qingdao, 266590, P.R. China. [2]Science and Technology on Electronic Test & Measurement Laboratory, North University of China, Taiyuan, 030051, P. R. China. [3]National Synchrotron Radiation Laboratory, University of Science and Technology of China, Hefei, 230029, P. R. China. [4]State Key Laboratory of High Performance Ceramics and Superfine Microstructure, Shanghai, 200050, P. R. China. Hengyang Qiao and Haiqing Sun contributed equally to this work. Correspondence and requests for materials should be addressed to F.S. (email: sf751106@sina.com.cn)
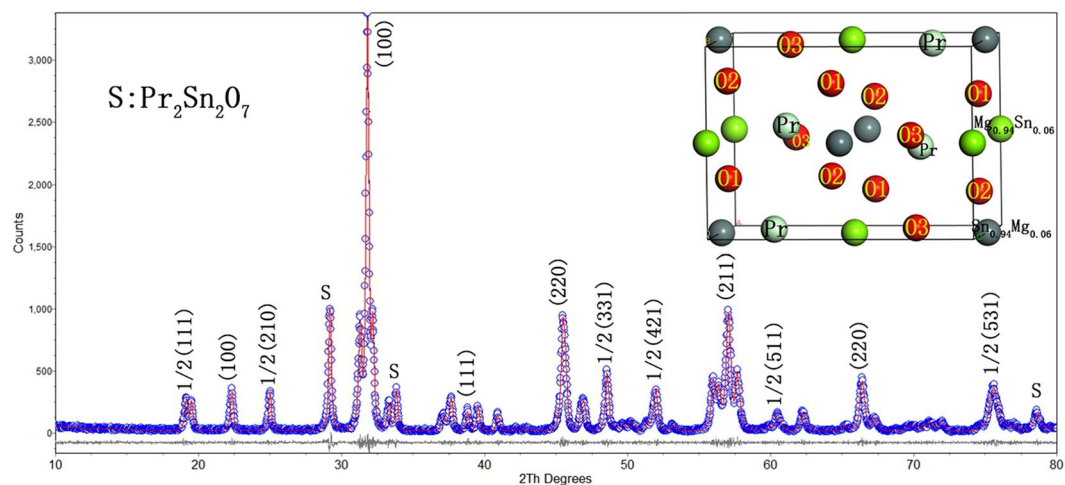
Figure 1. Observed XRD data (◯ marks) and calculated (red line) from Rietveld refinements of Pr(Mg$_{1/2}$Sn$_{1/2}$)O$_3$. The inset is the unit cell structure model of Pr(Mg$_{1/2}$Sn$_{1/2}$)O$_3$ ceramics.

Atom	Site	x	y	z	Ion	Occupation
Pr	4e	0.4859	0.5535	0.2502	Pr^{3+}	1
Mg1	2c	0	0.5	0	Mg^{2+}	0.94
Mg2	2d	0.5	0	0	Mg^{2+}	0.06
Sn1	2d	0.5	0	0	Sn^{4+}	0.94
Sn2	2c	0	0.5	0	Sn^{4+}	0.06
O1	4e	0.298	0.295	0.05	O^{2-}	1
O2	4e	0.199	0.808	0.061	O^{2-}	1
O3	4e	0.606	−0.032	0.257	O^{2-}	1

Table 1. The Position of Each Element Atom of Pr(Mg$_{1/2}$Sn$_{1/2}$)O$_3$ ceramics.

Here, in this work, PMS ceramic was synthesized through a conventional solid-state sintering technique. X-ray diffraction, and vibrational spectra (Raman and FTIR spectroscopies) were determined. We also used the four-parameter semi-quantum (FPSQ) model to calculate the intrinsic properties (dielectric constant and loss), which were compared with the data calculated by the Clausius-Mosotti equation (molecular polarizabilities), as well as the relationship between the damping coefficient and the intrinsic dielectric loss. The effect of the IR modes to the dielectric properties were analyzed. The Kramers–Krönig (K–K) analysis was conducted to acquire the real and imaginary parts of the dielectric constant for examine the vibrator parameters of PMS ceramic. This work may provide a basis of future research on the crystal structures, phone modes and intrinsic properties of rare-based $A(B'_{1/2}B''_{1/2})O_3$-type MWDCs.

Experiment

Pr(Mg$_{1/2}$Sn$_{1/2}$)O$_3$ ceramics was prepared using a conventional solid-state reaction method. Pr$_2$O$_3$, MgCO$_3$, and SnO$_2$ powders with purity of 99.9% were used as raw materials with stoichiometric Pr:Mg:Sn = 2:1:1 molar ratio in polyethylene jars with zirconia balls for 4 h, next dried, and then calcined at 1200 °C for 4 h. After re-milling for 4 h, these mixed powders were dried and pressed into discs of 15 mm × 1 mm, and at last, sintered at 1500 °C for 4 h. The surfaces of the samples were carefully polished using micron-scale Al$_2$O$_3$ powder, and they were rubbed off about 20 micrometers before testing X-ray diffraction, and vibrational spectra.

XRD was conducted using a Rigaku D/max-rB X-ray diffractometer with Cu-K_α incident source within the 10°–80° 2θ range (0.02°, 2θ step size, and 1 s per step). Raman scattering spectra was obtained at room temperature by using a Nexus 670 spectrometer equipped with a liquid-N$_2$-cooled CCD detector and an Olympus BXL microscope (100 × and 20 × objectives). Measurements were obtained in back-scattering geometry by using a Pr:YVO$_4$ laser at 514 nm line as the excitation source (10 mW). Accumulation times were typically 10 collections at an interval of 5 s, and the spectral resolution was greater than 2 cm^{-1}. The FTIR spectra were obtained at room temperature by using a Bruker IFS 66 v FTIR spectrometer with a highly sensitive DTGS detector. The laser source was He–Ne.

Results and Discussion

The XRD pattern after Rietveld refinement of the sample is presented in Fig. 1, which shows the main crystalline phase is PMS with double perovskite structure (monoclinic crystal system). The crystal structure model is shown
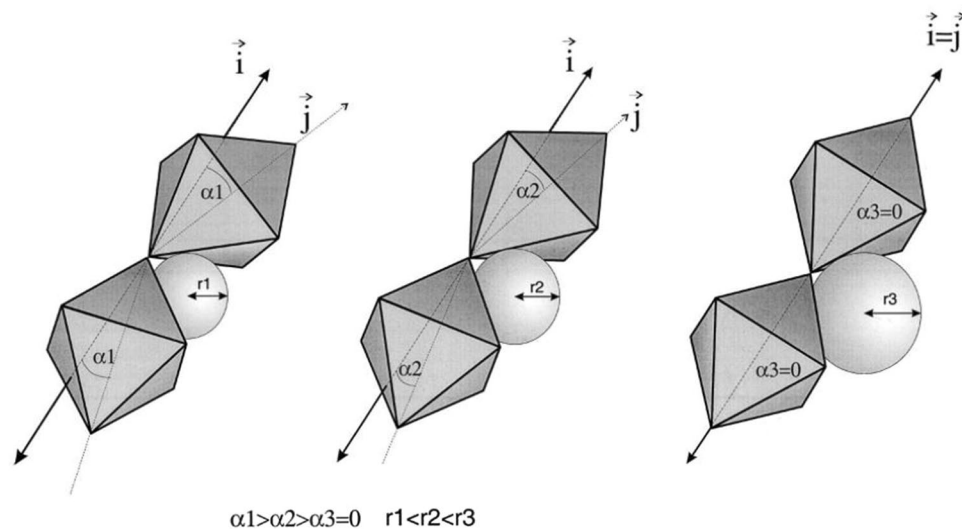
α1>α2>α3=0   r1<r2<r3

Figure 2. Schematic presentation of the correlation between tilt angles and A-site ionic radii (α1 > α2 > α3 = 0 r1 < r2 < r3)[22].

in the top right corner of Fig. 1, whose crystal structure data are listed in Table 1. Some second phases, including $Pr_2Sn_2O_7$ (JCPDS Card No. 13–0184, marked as S), are observed, due to the volatilization of magnesium.

A series of extra peaks was indexed by using half-integer Miller indices, such as 1/2(111), which correspond to superlattice reflection peaks. According to Glazer[20], superlattice reflection peaks, with specific combinations of odd (o) and even (e) miller indices, can indicate the distortion type of crystal structure, such as octahedral in-phase tilting (ooe, oeo, eoo), octahedral anti-phase tilting (ooo, h + k + l > 3), the chemical order (ooo) and anti-parallel displacement of A-site cation (eoe, eeo, oee) etc. Here, o and e denote the odd number (o) and even number (e) in Miller index, respectively.

The extra superlattice peaks originate from the ordered arrangement of cations in the B-site. The diffraction peaks (1/2(210), 1/2(421) and 1/2(432)) are related to the cations in A-site, and the diffraction peaks (1/2(331) and 1/2(511)) are related to the anti-phase tilting of the octahedron. The existence of the diffraction peak 1/2(111) is the obvious evidence of the B-site cations 1:1 ordering. In addition, the splitting of diffraction peaks, such as peak (110) and peak (111), are observed, which indicates that the symmetry decreases.

For octahedral tilting, according to the following Eq. (1)[21]:

$$t = \frac{r_A + r_O}{\sqrt{2}\,(r_B + r_O)}$$

(1)

The tolerance factor (t), where r_A, r_B and r_O are the radii of the A-, B-site and O-ion, respectively. That is, the tolerance factor is positively related to the parameter of r_A. The smaller of the tolerance factor (t), the larger the octahedral tilting. Figure 2 is the schematic presentation of the correlation between tilt angles and A-site ionic radii, referred by ref.[22]. Obviously, with the A-site ion radii decreases, the degree of octahedral tilting increases.

The Rietveld refinement results are listed in Table 2, which indicates $P2_1/n1$ space group of the PMS sample.

Figure 3 is the Raman scattering spectrum of PMS ceramic with Raman shifts from $50\,cm^{-1}$ to $900\,cm^{-1}$, which distinguishes 9 Raman active modes for the sample. According to group theory analysis, there are 24 ($12A_{1g} + 12B_{1g}$)[13] predicted Raman active modes for the phase-pure PMS. The Raman-active modes of ceramic with cubic $Fm\bar{3}m$ structure is ($A_{1g} + 2F_{2g} + E_g$)[23], and B-site 1:1 ordered structure can present four intense Raman active modes with A_{1g}, $2F_{2g}$, and E_g symmetries. Here, we cannot identify all the 24 Raman active modes due to the mutual influence of the Raman active vibration modes and resolution of the measuring instrument.

When the excitation light interacts with the sample molecules, the energy exchange occurs after the collision of the photon with the sample molecules, and the photon obtains part of the energy from the sample molecules. So that the frequency of light is changed. Raman shift is the difference between the scattered light frequency and the incident light frequency.

The greater the molecular bond energy is, the greater the energy can get when the photon collides with the molecule, and the greater the Raman shift. The bond energy is mainly affected by the bond length, and the longer the bond length, the smaller the bond energy. In short, the longer the bond length, the lower the Raman shift, that is, Raman shifts are profoundly influenced by the bond lengths, and the bond length values of the $Pr(Mg_{1/2}Sn_{1/2})O_3$ ceramic were illustrated in Table 3.

In Fig. 3, the modes of 1~4 within the range of 110–200 cm^{-1} are derived from F_{2g} vibration (A-site cations, part I). The modes within the range of 300–420 cm^{-1}, *i.e.*, modes 5, 6, and 7, correspond to the 1:1 ordered phase in B-sites (part II). The other two modes, 8 and 9, correspond to the vibration of oxygen atoms. The mode with the highest Raman shifts (above 650 cm^{-1}) is attributed to the A_{1g}-like mode, which corresponds to the symmetric breathing of oxygen octahedra because of the displacement of oxygen atoms along the Mg–O–Sn axis, whose frequency is primarily determined by the distances and bonding forces of Mg–O and Sn–O bonds[24]. The FWHM

Formula	Pr(Mg$_{1/2}$Sn$_{1/2}$)O$_3$
Crystal system	Monoclinic
Space group	$P121/n1$
a (Å)	5.5713191
b (Å)	5.7226529
c (Å)	7.9533907
Cell volume (Å^3)	253.57549
Z	4
Software	Topas3
Radiation	Cu $K\alpha$
Temperature (K)	293
Profile range in degree	$10 \leq 2 \leq 80°$
No. of data points	5501
R-factor:	
R_p	7.02
R_{wp}	10.33
R_{exp}	9.01
R-Bragg	0.664

Table 2. Crystallographic Data of Pr(Mg$_{1/2}$Sn$_{1/2}$)O$_3$ Derived from Rietveld Refinement of XRD Data.

Bond type	D$_{-ave}$(Å)
Pr-O	2.5482
Mg-O	2.0788
Sn-O	2.0788
O-O	2.9510

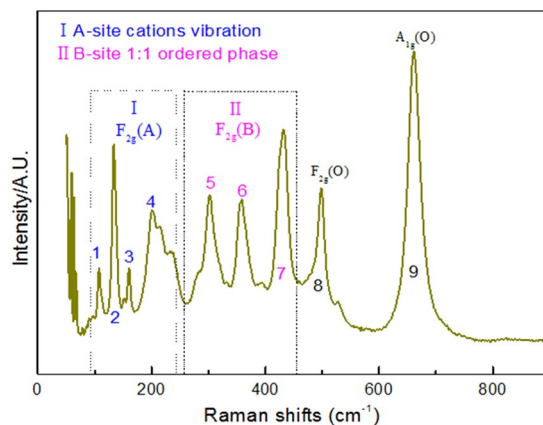**Table 3.** Bond length of the Pr(Mg$_{1/2}$Sn$_{1/2}$)O$_3$ ceramics.

Figure 3. The Raman Spectra of PMS Ceramics in the range 50 cm^{-1} to 900 cm^{-1}.

of the A_{1g} vibration mode is related to the B-site cation ordering[13], i.e., B-O$_6$ octahedron for O^{2-} ions in O1 and O2. The Raman spectrum with active modes can be fitted with Lorentzian function to obtain the full width at half maximum (FWHM); the values are listed in Table 4.

The far-infrared reflection spectra of Pr(Mg$_{1/2}$Sn$_{1/2}$)O$_3$ ceramics is shown in Fig. 4 with the wavenumber from 40 cm^{-1} to 700 cm^{-1}. According to the group theory analysis[25], the MWDCs with space group of $P2_1/n1$ have 33 infrared active vibration mode ($17A_u + 16B_u$), and the vibrational modes of A_u and B_u cannot split because the anisotropy tends to be balanced. Therefore, the number of the effective infrared active vibration mode of ceramic sample is 17[13]. In the far infrared reflectance spectrum, different vibrational modes correspond to different reflection bands. However, due to the instrument resolution and the mutual influence between vibration modes, it is difficult to distinguish all the reflection bands of 17 vibration modes, and only 7 reflection bands can be distinguished obviously, as shown in Fig. 4.

Modes	Frequency (cm⁻¹)	FWHM (cm⁻¹)
1 $F_{2g}(A)$	107.71	2.32
2	132.99	1.14
3	159.15	2.19
4	201.57	4.56
5 $F_{2g}(A)$	303.08	4.23
6	357.88	4.78
7	431.74	4.16
8 $F_{2g}(O)$	497.69	3.94
9 $A_{1g}(O)$	660.15	3.56

Table 4. The phonon modes parameters (Frequencies and FWHM values) from Raman spectra.
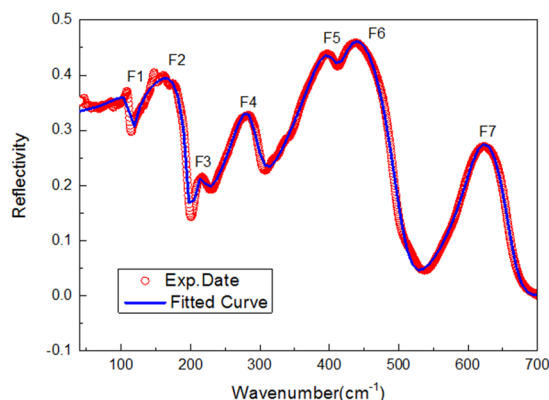

Figure 4. The FT-IR reflection spectrum of $Pr(Mg_{1/2}Sn_{1/2})O_3$.

According to Eq. (3.2) in ref.[26], the relationship between the dielectric constant and the frequency is inversely proportional. The curve is fitted by using the Lorentz FPSQ models to extract the vibrational frequencies of the IR modes. The vibrational frequencies of the IR modes were extracted by fitting the curve with Lorentz FPSQ models. These models describe the correlation between the complex permittivity (ε^*) and vibrational modes of the ceramic materials, as follows Eq. (2):

$$\varepsilon^*(\omega) = \varepsilon'(\omega) - i\varepsilon''(\omega) = \varepsilon\infty \prod_{j=1}^{n} \frac{\Omega_{jLO}^2 - \omega^2 + i\omega\gamma_{jLO}}{\Omega_{jTO}^2 - \omega^2 + i\omega\gamma_{jTO}} \tag{2}$$

(Four-parameter model)

$$R = \left| \frac{\sqrt{\varepsilon^*} - 1}{\sqrt{\varepsilon^*} + 1} \right|^2 \tag{3}$$

Where ε_∞ refers to the optical permittivity, and n is the number of vibrational modes. Ω_{jTO}, γ_{jTO}, and Ω_{jLO}, γ_{jLO} are the frequencies and damping factors of the jth transverse and longitude modes of vibration, respectively. The Fresnel equation [Eq. (3)] describes the relationship between the IR reflection spectrum and complex permittivity. Reflectivity (R) is an important parameter in the infrared reflectance spectrum. According to the Eq. (2) and the classical Kramers–Krönig (K-K) relation, the real part ε' and the imaginary part ε'' of the dielectric constant were calculated from the fitted spectra.

According to the results of four parameters fitting, the influence of each vibration mode on dielectric properties (permittivity ε_j and loss $\tan\delta_j/\omega$) is analyzed and discussed. The dielectric parameters can be calculated from Eqs (4) and (5), as follows:

$$\varepsilon_j = \frac{\varepsilon\infty}{\Omega_{jTO}^2} \frac{\prod_K (\Omega_{kLO}^2 - \Omega_{jTO}^2)}{\prod_{k \neq j} (\Omega_{kTO}^2 - \Omega_{jTO}^2)} \tag{4}$$

$$\tan\delta j/\omega = \frac{\varepsilon j\gamma/\Omega_{jTO}^2}{\varepsilon\infty + \sum_j \varepsilon j} \tag{5}$$

The calculated ε_j and $\tan\delta_j/\omega$ are also listed in Table 5. The vibrational modes at lower frequencies yield a larger contribution to the permittivity (ε_j) and loss ($\tan\delta_j/\omega$). Thus, the dielectric properties are greatly affected

Number	modes	Ω_{cal} (cm^{-1})	Ω_{jTO} (cm^{-1})	γ_{jTO} (cm^{-1})	Ω_{jLO} (cm^{-1})	γ_{jLO} (cm^{-1})	$\Delta\varepsilon_j$	$\tan\delta_j/\omega$ (10^{-4}cm)
1	$F_{1u}^{(1)}$	108	114.79	17.88	115.56	12.58	0.24	0.236
2	$F_{2u}^{(2)}$	161	176.28	80.69	199.48	11.99	4.73	8.962
3	$F_{3u}^{(3)}$	216	206.00	21.09	220.10	46.53	0.41	0.147
4	$F_{4u}^{(4)}$	284	281.25	39.02	299.37	42.89	1.10	0.396
5	$F_{5u}^{(5)}$	398	387.85	68.23	411.66	35.07	2.28	0.755
6	$F_{6u}^{(6)}$	438	417.94	41.47	506.73	49.72	0.46	0.079
7	$F_{7u}^{(7)}$	623	606.14	54.47	665.02	36.90	0.40	0.043

Table 5. Parameters of the IR-Active Modes for the Four-Parameter Model. $\varepsilon_\infty = 4.10$.

by the modes involving more movements of heavier metal atoms. The first mode $F_{1u}^{(1)}$ can be assigned to the 1:1 ordered phase in B-sites. $F_{2u}^{(2)}$ also provides larger contribution to the dielectric constant and loss of a material than the other modes, which is mainly performed as the inverted translational vibration of Pr-MgO$_6$ octahedron. Within the range of 200–500 cm^{-1} [$F_{3u}^{(3)}$, $F_{4u}^{(4)}$, $F_{5u}^{(5)}$ and $F_{6u}^{(6)}$], the vibrational modes correspond to the stretching vibrations of Mg–O–Sn. Within the range of 500–700 cm^{-1}, $F_{7u}^{(7)}$ is regarded as the bending vibrations of Sn–O$_6$. The permittivity and dielectric loss of PMS ceramics can be obtained by determining the sum of ε_j and $\tan \delta_j/\omega$ of all the modes.

The permittivity value (ε_r) of IR fitting obtained by determining the sum of ε_j of all the modes is 13.72, and the calculated dielectric loss is $\sum\tan(\delta j)/\omega = 1.062 \times 10^{-3}$.

The dielectric constant of PMS ceramics can also be calculated by Clausius-Mossi equation. According to the additivity rule of molecular polarizabilities, the molecular polarizability of the PMS ceramics can be obtained by adding the molecular polarizabilities of several simple substances, as shown in the following Eq. (6):

$$\alpha\left(Pr(Sn_{1/2}Mg_{1/2})O_3\right) = \alpha(Pr^{3+}) + \frac{1}{2}\alpha(Sn^{4+}) + \frac{1}{2}\alpha(Mg^{2+}) + 3\alpha(O^{2+}) \tag{6}$$

The single ion polarizability can be obtained from the research of Shannon R D[26]. Based on the molecular polarizability, the dielectric constant calculated by Clausius-Mossoi equation is 13.93, which is similar to the value of 13.72 by four-parameter fitting.

The quality factor Q is a basic measure of the energy loss in the microwave dielectric ceramic system and it is negatively correlated with the dielectric loss ($Q = 1/\tan \delta$). The dielectric loss mechanism includes the extrinsic loss associated with the preparation process and the intrinsic loss associated with the crystal structure.

The non-intrinsic loss can be effectively reduced by adjusting the preparation parameters. The intrinsic loss is sensitive to the micro-structure information, which is related to the vibration mode of the lattice. The intrinsic loss can be expressed as follows Eq. (7):

$$\tan \delta = \left(\frac{\gamma}{\omega_T^2}\right)\omega_0 \tag{7}$$

Where ω_T is the angular frequency of lattice vibration transverse optical mode, γ is the damping factor of the material. The classical radiation theory points out that the Full Width at Half Maximum (FWHM) of the Raman spectrum is closely related to the frequency and damping, and the damping coefficient can be calculated according to the following Eq. (8):

$$FWHM = \gamma\sqrt{\gamma^2 + 4\omega_0^2}/2\omega_0 \tag{8}$$

Where γ is the damping factor and ω_0 is the spectral center frequency. According to the Eq. (7) and Eq. (8), the second peak of the vibration mode $F_{2g}(A)$ in the Raman spectrum has the greatest influence on the intrinsic loss. The calculated intrinsic loss is 1.008×10^{-3}, which is almost the same as the value 1.062×10^{-3} obtained by four-parameter fitting.

The imaginary and real part of the PMS ceramics complex dielectric constant $\varepsilon(\omega) = \varepsilon'(\omega) + i\varepsilon''(\omega)$ can describe the characteristics of electromagnetic wave absorption of phonons. In Fig. 4, PMS ceramics infrared spectra were K-K conversion, and calculate the PMS ceramics complex dielectric constant $\varepsilon(\omega) = \varepsilon'(\omega) + i\varepsilon''(\omega)$. The imaginary part $\varepsilon''(\omega)$ and real part $\varepsilon'(\omega)$ of the dielectric constant are analyzed in detail. Figure 5 is the real part of dielectric constant $\varepsilon'(\omega)$ image of PMS ceramics after K-K conversion.

The real part $\varepsilon'(\omega)$, which is a function of wavelength, ranges from 40 cm^{-1} to 680 cm^{-1} (Fig. 5). For ε' of the PMS ceramics, seven peaks are shown in Fig. 5. Each peak is numbered from low to high frequency. The real part is the common dielectric constant and related to the dielectric properties. For $\varepsilon' = \frac{(\varepsilon_s - \varepsilon_\infty)\varepsilon_T^2\gamma}{\varepsilon[4(\varepsilon_T - \varepsilon)^2 + \gamma^2]}$, the resonant frequency ω_{TO} of the vibrator can be determined from the real part of the dielectric constant when $\varepsilon'(\omega)$ reaches the maximum. Among these seven modes, No. 7 reaches the maximum value of the real part.

As shown in Fig. 6, for PMS ceramics imaginary part of dielectric constant $\varepsilon''(\omega)$ image can be clearly observed in 6 different modes of vibration. Each peak is numbered from low to high frequency, as in No. 1~6. The electromagnetic wave absorption characteristics of the vibrator are characterized by imaginary parts. These peaks are obtained through Lorentz fitting, and each peak corresponds to an IR-active mode.
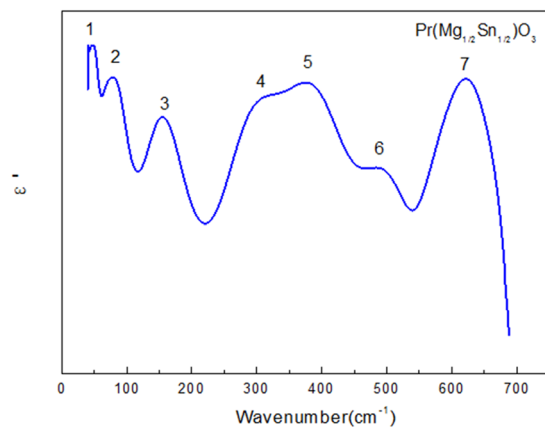
Figure 5. The real part of dielectric constants $\varepsilon'(\omega)$ calculated from K-K analysis for the $Pr(Mg_{1/2}Sn_{1/2})O_3$ ceramics.
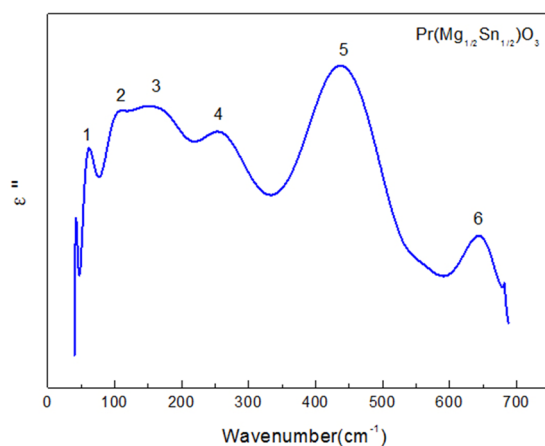

Figure 6. The imaginary part of dielectric constants $\varepsilon''(\omega)$ calculated from K-K analysis for the $Pr(Mg_{1/2}Sn_{1/2})O_3$ ceramics.

Conclusion

The $Pr(Mg_{1/2}Sn_{1/2})O_3$ ceramics were prepared through a conventional solid-state reaction method at 1500 °C for 4 h. The crystal structure was investigated through XRD, and the vibrational phone modes were investigated by Raman and FTIR reflection spectroscopies. The refinement plot of the XRD shows that the material exhibits a monoclinic double perovskite structure ($P2_1/n1$). PMS is the main crystalline phase, which is accompanied by a small amount of $Pr_2Sn_2O_7$ as the second phase. The Raman spectrum was obtained, and the highest Raman shifts mode above 660.9 cm^{-1} is attributed to the $A_{1g}(O)$-like mode, which corresponds to the symmetric stretching of oxygen octahedron. The four modes within the range of 110–200 cm^{-1} are derived from the F_{2g} vibrations (A-site cations), and the other three modes (300–430 cm^{-1}) are derived from the F_{2g} vibrations (B-site cations). The intrinsic loss (tan δ_j/ω) calculated by FPSQ was 1.062×10^{-3}, which agree well with the value of 1.008×10^{-3} calculated baed on damping coefficient and center frequency of optical mode. Through calculation and comparison, the second peak of the vibration mode $F_{2g}(A)$ in the Raman spectrum has the greatest influence on the intrinsic loss. We assigned the IR-active modes as F_1 (108 cm^{-1}), F_2 (161 cm^{-1}), F_3 (216 cm^{-1}), F_4 (284 cm^{-1}), F_5 (398 cm^{-1}), F_6 (438 cm^{-1}), and F_7 (623 cm^{-1}). Almost all of the atoms are involved in each IR vibrational mode, but each atom exhibits different effects. These data indicate that the vibrational modes at lower frequency ($F_{2u}^{(2)}$) provide larger contribution in terms of ε_j and tanδ_j/ω. Thus, dielectric properties are mostly affected by modes involving more movements of heavier metal atoms, *i.e.*, the inverted translational vibration of Pr-MgO_6 octahedron. The permittivity value (ε_r) of IR fitting obtained by determining the sum of ε_j of all the modes is 13.72, which agrees well with the permittivity value of 13.93 calculated by Clausius-Mossoi equation.

References

1. Chen, Y. C. & Li, C. H. Improvement in microwave dielectric properties of La(Mg0.5Sn 0.5)O3 ceramics by applying ZnO–B2O3–SiO2. *Journal of Materials Science: Materials in Electronics* **25**, 4312–4318 (2014).
2. Lee, D. Y. *et al.* Crystal structure and microwave dielectric properties of La(Mg1/2Ti1/2)O3 ceramics. *Journal of Materials Science Letters* **19**, 131–134 (2000).
3. Khamoushi, K. & Arola, E. Structural and Dielectric Properties of (La, Nd) (Mg1/2Ti1/2)O3 Perovskites. *Physics* **88**, 667–670 (2015).

4. Sun, X. *et al.* Enhanced dielectric and tunable properties of barium strontium titanate thin films through introducing Nd(Zn 1/2 Ti 1/2)O 3 and adjusting Ba/Sr. *Journal of Materials Science* **49**, 1058–1065 (2014).
5. Sebastian, M. T. Dielectric Materials for Wireless Communication (2015).
6. Shi, F., Liang, K. & Qi, Z. M. Investigation of the crystal structure, lattice vibration and dielectric property of SrZrO3 ceramic. *Journal of Materials Research* **31**, 3249–3254 (2016).
7. Shi, F., Sun, H., Wang, J. & Zhang, J. Effects of calcining temperature on crystal structures, dielectric properties and lattice vibrational modes of Ba(Mg 1/3Ta 2/3)O3 ceramics. *Journal of Materials Science: Materials in Electronics* **27**, 5383–5388 (2016).
8. Salak, A. N., Prokhnenko, O. & Ferreira, V. M. Temperature evolution of the crystal structures in La(Mg1/2Ti1/2)O3 perovskite: relation to the microwave dielectric properties. *Journal of Physics Condensed Matter* **20**, 2905–2910 (2008).
9. Chen, Y.-C., Wang, S.-C. & Chen, K.-H. Effect of B2O3 Additions and Sintering Temperature on Microwave Dielectric Properties of (1−x)La(Mg0.5Sn0.5)O3-xCa0.8Sr0.2TiO3 Ceramic. *Ferroelectrics Letters Section* **37**, 90–100 (2010).
10. Babu, G. S. *et al.* Far-infrared, Raman spectroscopy, and microwave dielectric properties of La(Mg 0.5 Ti (0.5−x) Sn x)O3 ceramics. *Journal of Applied Physics* **102**, 064906-064906-064907 (2007).
11. Babu, G. S., Subramanian, V., Murthy, V. R. K., Moreira, R. L. & Lobo, R. P. S. M. Crystal structure, Raman spectroscopy, far-infrared, and microwave dielectric properties of (1−x)La(MgSn)0.5O3–xNd(MgSn)0.5O3 system. *Journal of Applied Physics* **103**, 084104–084104 (2008).
12. Chen, Y.-C. & Chang, Y.-H. Dielectric properties of B2O3-doped La(Mg0.5Sn0.5)O3 ceramics at microwave frequencies. *Journal of Alloys and Compounds* **477**, 450–453, https://doi.org/10.1016/j.jallcom.2008.10.032 (2009).
13. Chen, Y., Tsai, R. & Wang, Y. Dielectric Properties of B2O3-Doped Nd(Mg0.5Sn0.5)O3 Ceramics at Microwave Frequencies. *Journal of Alloys & Compounds* **477**, 450–453 (2009).
14. Chen, Y. C. Improved Microwave Dielectric Properties of La(Mg0.5Sn0.5)O3 Ceramics with Yb3+ Doping. *International Journal of Applied Ceramic Technology* **9**, 606–614 (2012).
15. Chen, Y.-C., Chang, K.-C. & Yao, S.-L. Improved microwave dielectric properties of Nd(Mg0.5Sn0.5)O3 ceramics by substituting Mg2+ with Zn2+. *Ceramics International* **38**, 5377–5383, https://doi.org/10.1016/j.ceramint.2012.03.047 (2012).
16. Chen, Y. C. & Chen, K. C. Dielectric Properties of La(Mg 0.5 Sn 0.5)O3 Ceramics Doped with V 2 O 5 at Microwave Frequencies. *Ferroelectrics* **393**, 54–62 (2009).
17. Martin, C., Maignan, A. & Raveau, B. Effect of aluminium for manganese substitution upon the GMR properties of the praseodymium manganites. *Journal of Materials Chemistry* **6**, 1245–1248 (1996).
18. Pan, K. L., Chen, M. C., Yu, S. J., Yan, S. Y. & Chang, M. B. Enhancement of nitric oxide decomposition efficiency achieved with lanthanum-based perovskite-type catalyst. *Journal of the Air & Waste Management Association* **66**, 619 (2016).
19. Ullmann, H., Trofimenko, N., Tietz, F., Stöver, D. & Ahmad-Khanlou, A. Correlation between thermal expansion and oxide ion transport in mixed conducting perovskite-type oxides for SOFC cathodes. *Solid State Ionics* **138**, 79–90 (2000).
20. Glazer, A. M. Simple ways of determining perovskite structures. *Acta Crystallographica* **31**, 756–762 (1975).
21. Reaney, I. M. & Ubic, R. Dielectric and structural characteristics of perovskites and related materials as a function of tolerance factor. *Ferroelectrics* **228**, 23–38 (1999).
22. Valant, M., Suvorov, D. & Rawn, C. Intrinsic Reasons for Variations in Dielectric Properties of $Ba_{6-3x}R_{8+2x}Ti_{18}O_{54}$(R=La–Gd) Solid Solutions. *Japanese Journal of Applied Physics* **38**, 2820–2826 (1999).
23. Colla, E. L., Reaney, I. M. & Setter, N. Effect of Structural-Changes in Complex Perovskites on the Temperature-Coefficient of the Relative Permittivity. *Journal of Applied Physics* **74**, 3414–3425 (1993).
24. Liegeois-Duyckaerts, M. Vibrational studies of molybdates, tungstates and related c compounds—III. Ordered cubic perovskites A2BIIBVIO6. *Spectrochimica Acta Part A Molecular Spectroscopy* **30**, 1771–1786 (1974).
25. Santos, C. C. *et al.* Raman investigations of rare earth orthovanadates. *Journal of Applied Physics* **101**, 155 (2007).
26. Arulsamy, A. D. Renormalization group method based on the ionization energy theory. *Annals of Physics* **326**, 541–565 (2008).
27. Shannon, R. D. Dielectric polarizabilities of ions in oxides and fluorides. *Journal of Applied Physics* **73**, 348–366 (1993).

Acknowledgements

Author Contributions

Jianzhu Li, Huiling Chen, Chao Xing and Ze-Ming Qi carried out the experimental work and the data collection and interpretation. Jing Wang and Xunqian Yin participated in the design and coordination of experimental work, and acquisition of data. Jun Yang and Helei Dong participated in the study design, data collection, analysis of data and preparation of the manuscript. Hengyang Qiao, Sunhai Qing and Feng Shi carried out the study design, the analysis and interpretation of data and drafted the manuscript. All authors read and approved the final manuscript.

Additional Information

Competing Interests: The authors declare that they have no competing interests.

Publisher's note: Springer Nature remains neutral with regard to jurisdictional claims in published maps and institutional affiliations.